A C-Band Wind/Rain Backscatter Model

Congling Nie, *Student Member, IEEE*, and David G. Long, *Senior Member, IEEE*

***Abstract*—With the confirmed evidence of rain surface perturbation in recent studies, the rain effects on C-band scatterometer measurements are reevaluated. By using colocated Tropical Rainfall Measuring Mission Precipitation Radar, ESCAT on European Remote Sensing Satellites, and European Centre for Medium-Range Weather Forecasts data, we evaluate the sensitivity of C-band σ° to rain. We develop a low-order wind/rain backscatter model with inputs of surface rain rate, incidence angle, wind speed, wind direction, and azimuth angle. We demonstrate that the wind/rain backscatter model is accurate enough for describing the total backscatter in raining areas with relatively low variance. We also show that the rain surface perturbation is a dominating factor of the rain-induced backscatter. Using three distinct regimes, we show under what conditions the wind, rain, and both wind and rain can be retrieved from the measurements. We find that the effect of rain has a more significant impact on the measurements at high incidence angles than at low incidence angles.**

***Index Terms*—Backscatter, European Centre for Medium-Range Weather Forecasts (ECMWF), European Remote Sensing (ERS), rain, scatterometer, surface effects, Tropical Rainfall Measuring Mission (TRMM) Precipitation Radar (PR).**

I. Introduction

DATA from the C-band wind scatterometer of the active microwave instrument (ESCAT) on the European Remote Sensing (ERS) satellites, launched by the European Space Agency in 1991 (ERS-1) and 1995 (ERS-2), have been used to estimate wind velocity and direction over the ocean. Unlike Ku-band, the C-band scatterometer signal is traditionally considered rain transparent. It is reported that the radar backscattering by raindrops for the C-band signal is negligibly small and the attenuation exceeds 1 dB only when the rain rate is above 50 mm/h [1], [2]. However, recent studies reveal that surface effects by rain may significantly modify the total backscatter of both Ku-band and C-band scatterometers [3]–[5], and hence influence the wind retrieval process. Therefore, evaluating the various surface effects of rain on ERS scatterometer measurements is necessary for improving the accuracy of ERS wind estimation in raining areas. Furthermore, under some conditions, it may be possible to retrieve rain-rate information from the C-band scatterometer measurements.

For fair weather conditions (average sea state and absence of rain), scatterometer backscatter is mainly from wind-driven gravity capillary waves (Bragg waves). The normalized radar backscattering cross section (σ°) is related to wind velocity and wind direction through an empirical model known as the geophysical model function (GMF). Wind retrieval is based on the inversion of the GMF [6]. Ambiguities exist due to the shape of the GMF. In order to eliminate ambiguities, multiple σ° measurements at different azimuth angles are collected and used in wind retrieval.

In a raining area, the wind-induced scatterometer backscatter signature is altered by rain. Rain striking the water creates splash products including rings, stalks, and crowns from which the signal scatters [7]. The contribution of each of these splash products to the backscattering varies with incidence angle and polarization. At VV-polarization, rain-generated ring-waves are the dominant feature for radar backscattering at all incidence angles. At HH-polarization, with increasing incidence angles, the radar backscatter from ring-waves decreases while the radar backscatter from nonpropagating splash products increases [4]. Similar results are found in experiments done with a VV-polarized Ku-band system [7]. Raindrops impinging on the sea surface also generate turbulence in the upper water layer which attenuate the short gravity wave spectrum [5], [8]. A study by Melsheimer *et al.* [5] shows that the modification of the sea-surface roughness by impinging raindrops depends strongly on the wavelength of water waves: the net effect of the impinging raindrops on the sea surface is a decrease of the amplitude of those water waves which have wavelengths above 10 cm and an increase of the amplitude of those water waves which have wavelengths below 5 cm [5]. But, the critical transition wavelength at which an increase of the amplitude of the water wave turns into decrease is not well defined. It depends on the rain rate, the drop size distribution, the wind speed, and the temporal evolution of the rain event [5]. Thus, in the transition wavelength regime, raindrops impinging on the sea surface may increase or decrease the amplitude of the Bragg waves. In addition to the modification of the sea-surface roughness by the impact of raindrops, the sea-surface roughness is also affected by the airflow associated with the rain event [5]. The scatterometer signal is additionally attenuated and scattered by the raindrops in the atmosphere.

To evaluate the effect of rain on C-band ESCAT σ° observations, we use a simple phenomenological backscatter model, similar to the one used in developing a Ku-band wind/rain backscatter model for SeaWinds [3]. To estimate the rain-induced parameters of the model, we use colocated Precipitation Radar (PR) data from the Tropical Rainfall Measuring Mission (TRMM) satellite. Each colocated region contains the overlapping swaths in which the time difference between the TRMM PR time tags and the ERS time tags is less than ± 15 min. Since colocated regions between ESCAT and TRMM PR are relatively rare, we processed 16 months of data from August 1, 1999 to December 31, 2000. About 82 181 colocations are found in this period. To improve the accuracy of

Manuscript received May 12, 2006; revised September 26, 2006.

The authors are with the Department of Electrical and Computer Engineering, Brigham Young University, Provo, UT 84602 USA.

Color versions of one or more of the figures in this paper are available online at http://ieeexplore.ieee.org.

Digital Object Identifier 10.1109/TGRS.2006.888457

the estimated model parameters, we use only the colocated regions where the overlapping PR swath contains more than 2.5% of the measurements flagged as rain certain in the TRMM 2A25 files.

Before illustrating the derivation of the model, we describe the data in Section II. In Section III, we define the wind/rain model and estimate the model coefficients. In Section IV, we validate the wind/rain backscatter model and estimate the influence of rain using regimes. Conclusions are reached in Section V.

II. Data

To derive the wind/rain backscatter model, we use colocated ESCAT backscatter, rain data from TRMM PR, and predicted wind fields from European Centre for Medium-Range Weather Forecasts (ECMWF) [9]. We describe these data in this section.

ESCAT on the ERS-1 and ERS-2 satellites is designed to measure ocean winds. The C-band scatterometer collects σ° measurements at 5.3-GHz VV-polarization. After collecting backscatter measurements, wind retrieval is performed by inverting the GMF, based on multiple σ° measurements at different azimuth angles and incidence angles for each wind vector cell (WVC). To allow sufficient azimuthal diversity, ERS has three side-looking antennas with the beams pointed at angles of 45°, 90°, and 135° from the satellite ground track on the starboard side. The incidence angles of each antenna vary across the swath, between 22° and 56° for the fore and aft antenna, and between 18.2° and 42° for the midantenna [10]. The swath width of ESCAT is 500 km. The effective resolution of ESCAT is 50×50 km^2 [10]. The σ° measurements have a Hamming window spatial response function. Because measurements with different incidence angles may have different characteristics, it is necessary to analyze them separately.

The numerical weather prediction wind fields from ECMWF provide surface wind estimates without consideration of rain. We use the ECMWF-predicted winds to estimate the wind-induced σ°. The ECMWF winds are trilinearly interpolated (both in space and time) from a $1^\circ \times 1^\circ$ latitude–longitude grid with a temporal resolution of 6 h to the ESCAT data times and locations. ECMWF-predicted σ°, computed using the improved GMF CMOD5, is on average 0.08 dB lower than ESCAT-measured σ° [11]. This introduces a region-dependent bias ϵ, which is estimated in Section III.

TRMM PR data are used to estimate rain. The TRMM satellite was launched in 1997 and orbits at a low inclination angle of 35°, providing coverage of the tropics. The TRMM PR instrument on the TRMM satellite has a horizontal resolution at the ground of about 4 km and a swath width of 220 km [12]. The TRMM PR antenna scans within 17° of the nadir. The latitudes of TRMM PR measurements are between ±36° [12]. Because both the viewing geometry and the operating frequency (13.8 GHz for TRMM PR versus 5.3 GHz for ESCAT) of TRMM PR and ESCAT are not the same, the effects of rain on the backscatter (atmospheric attenuation and backscattering) are different. We estimate the atmospheric effects of rain on the ESCAT signal by using the 3-D rain-rate estimation from TRMM PR level 2A25 product [13]. The colocation geometry of the TRMM PR and ESCAT on ERS are shown in Fig. 1. Due to the different orbit geometry and the narrow swath of ESCAT and TRMM PR, the colocations are relatively rare.

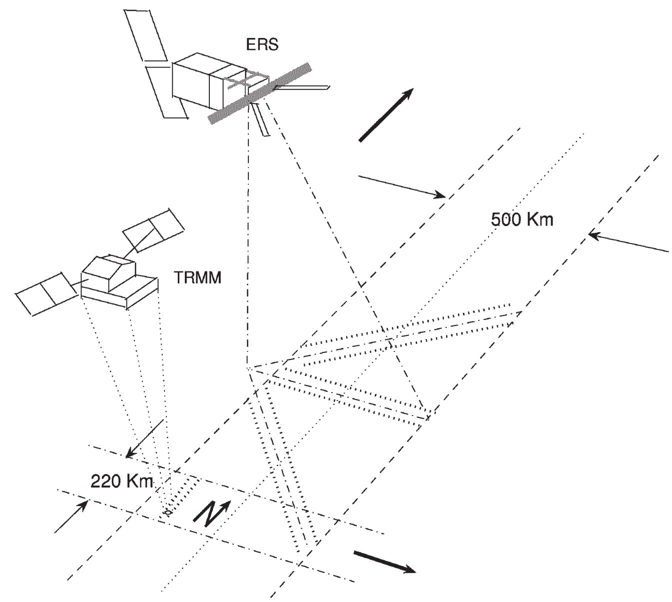

Fig. 1. Swath geometry of the TRMM PR and ESCAT on ERS instruments in colocating regions.

III. Model-Measured σ° in Rain and Wind

Rain drops impinging on the sea surface, airflow associated with rain roughening the sea surface, and rain-generated turbulence affect the surface backscattering of the scatterometer signal. Since we only care about the bulk effect of rain on the Bragg wave field, we combine all these contributions together into a single rain surface perturbation backscatter term $\sigma_{\rm surf}$. Assuming that $\sigma_{\rm surf}$ is additive with the wind-induced surface backscatter, we use a simple additive model for the total backscatter, following the Ku-band wind/rain backscatter model in [3]. The rain-modified measured backscatter $\sigma_{\rm m}$ is

$$\sigma_{\rm m} = (\sigma_{\rm wind} + \sigma_{\rm surf})\alpha_{\rm atm} + \sigma_{\rm atm} \tag{1}$$

where $\sigma_{\rm m}$ is the ESCAT-measured σ°, $\sigma_{\rm wind}$ is the wind-induced surface backscatter predicted by the ECMWF, $\sigma_{\rm surf}$ is the rain-induced surface perturbation backscatter, $\alpha_{\rm atm}$ is the two-way rain-induced atmospheric attenuation, and $\sigma_{\rm atm}$ is the rain-induced atmospheric backscatter.

The wind/rain backscatter model can be further simplified by summing the attenuated surface perturbation and the atmospheric scattering terms, creating a single effective rain backscatter parameter $\sigma_{\rm eff}$. The combined rain effect model is [3]

$$\sigma_{\rm m} = \sigma_{\rm wind}\alpha_{\rm atm} + \sigma_{\rm eff} \tag{2}$$

where

$$\sigma_{\rm eff} = \sigma_{\rm surf}\alpha_{\rm atm} + \sigma_{\rm atm}. \tag{3}$$

The rain-induced backscatter and attenuation are related to the rain intensity r and incidence angle θ. The wind-induced backscatter is a function of wind speed s, wind direction d, azimuth angle χ, and incidence angle. Thus, the total backscatter σ_{m} can be expressed as a function F of these parameters

$$\sigma_{\mathrm{m}} = F(r, s, d, \chi, \theta). \tag{4}$$

There are two metrics for rain intensity: integrated rain rate (kilometers per millimeter per hour) and surface rain rate (millimeters per hour). Because the rain is not uniformly distributed along the slant path, these two metrics are nonlinearly related. In the Ku-band wind/rain backscatter model, integrated rain rate is used as the metric [3], since contributions of the rain-induced surface backscatter and the rain-induced atmospheric backscatter are comparable. For the C-band model, the rain-induced surface backscatter dominates the rain-generated backscatter, and thus, the surface rain rate (millimeters per hour) is selected as the rain intensity metric. Also, since the beam of TRMM PR and ESCAT only overlaps on the ocean surface, using surface rain rate is expected to introduce smaller errors than using integrated rain rate.

Because the spatial response function gain is not uniform over the ESCAT footprint, the contribution of rainfall varies with the location in the footprint. Thus, the ESCAT-observed surface rain is a weighted average of the surface rain. We define the weighted-averaging function as

$$P_{\mathrm{ESCAT}} = \frac{\sum_{i=1}^{N} G(i) P_{\mathrm{PR}}(i)}{\sum_{i=1}^{N} G(i)} \tag{5}$$

where P_{ESCAT} is the ESCAT-observed parameter, $G(i)$ is the ESCAT spatial response function gain at the ith PR measurement, N is the number of PR data points within ESCAT 3-dB antenna pattern contour, and $P_{\mathrm{PR}}(i)$ is the parameters corresponding to the ith PR measurements. To estimate ESCAT-observed surface rain rate $R_{\mathrm{surf(ant)}}$, the TRMM PR level 2A25 surface rain rate $R_{\mathrm{surf(PR)}}$ is averaged over the ESCAT footprint using (5). Due to nonuniform beam filling (NUBF) and the ESCAT nonuniform spatial response gain pattern, there is a difference between the ESCAT gain-weighted average surface rain rate and the uniform-weighted average rain rate. This beam-filling variability is also noted in the Ku-band scatterometer rain/wind backscatter model [3]. We estimate the NUBF effect on surface rain rate by computing the normalized error $\epsilon = (R_{\mathrm{surf(ant)}} - R_{\mathrm{surf(uni)}})/R_{\mathrm{surf(uni)}}$ between the antenna-weighted average rain rate $R_{\mathrm{surf(ant)}}$ and the uniform-weighted average rain rate $R_{\mathrm{surf(uni)}}$ for each ESCAT measurement. Although the PR-measured rain also contains beam-filling error, we ignore its effect for simplicity. The uniform-weighted average surface rain rate $R_{\mathrm{surf(uni)}}$ is computed by averaging the PR-measured surface rain rates $R_{\mathrm{surf(PR)}}$ within the 3-dB ESCAT footprint with uniform weights $G(i) = 1/N$. We calculate the statistics of ϵ with significant rain rates ($\geq$ 0.8 mm/h) for the entire colocated data set. The mean of ϵ is 0.002, which is negligible, while the standard deviation is 0.152. This suggests that the NUBF does not introduce bias to the rain-rate estimates, but it increases the variability of the estimates. A histogram of the antenna-weighted average surface rain rates $R_{\mathrm{surf(ant)}}$ of the colocated data set is shown in Fig. 2. It is noted that the maximum of $R_{\mathrm{surf(ant)}}$ is about 40 mm/h, while the mean is about 0.4 mm/h.

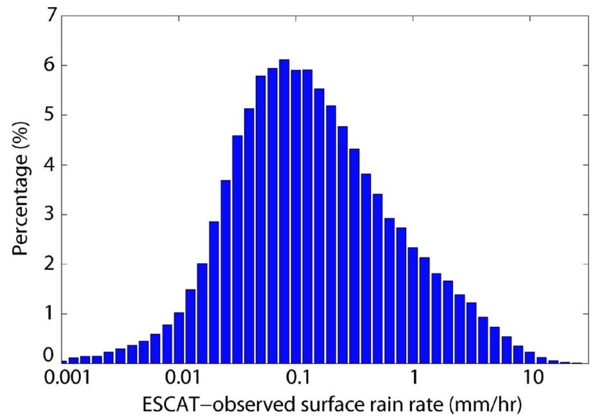

Fig. 2. Histogram of ESCAT response function weighted surface rain rate $R_{\mathrm{surf(ant)}}$ derived from TRMM PR observations of the colocated data set, consisting of 82 181 collocations with exceeding 2.5% rain certain over August 1, 1999 to December 31, 2000.

A. Estimating Model Parameters

To estimate the surface perturbation backscatter σ_{surf}, we need to know the rain-induced atmospheric backscatter σ_{atm}, the attenuation α_{atm}, and the wind-induced surface backscatter σ_{wind}. We estimate σ_{atm} and α_{atm} by using the colocated TRMM PR level 2A25 3-D rain rate.

To calculate the two-way atmospheric attenuation α_{atm}, we first estimate the atmospheric attenuation factor k_a at the ESCAT wavelength (5.7 cm) using the k_a–R relation, which relates k_a and the rain rate (mm/h) [14]

$$k_a = 2KR \ \mathrm{dB} \cdot \mathrm{km}^{-1}/\mathrm{mm} \cdot \mathrm{h}^{-1} \tag{6}$$

where $K = 0.0033$ for 5.7-cm wavelength and R is the TRMM PR level 2A25 3-D rain rate in millimeters per hour. Following the method in [3], the path integrated attenuation (PIA) in decibels at the ESCAT wavelength for each TRMM PR measurement $\mathrm{PIA}_{\mathrm{PR}}(i)$ is computed by integrating k_a through the PR antenna beam to the lowest no-surface-clutter range. The two-way atmospheric attenuation factor seen by ESCAT at the ith TRMM PR measurement $\alpha_{\mathrm{PR}}(i)$ is estimated by adjusting PR slant range to ESCAT slant range and converting $\mathrm{PIA}_{\mathrm{PR}}(i)$ to normal space

$$\alpha_{\mathrm{PR}}(i) = 10^{-\sec\theta_{(\mathrm{ESCAT})}\cos\theta_{(\mathrm{PR})}\mathrm{PIA}_{\mathrm{PR}}(i)/10} \tag{7}$$

where $\theta_{(\mathrm{ESCAT})}$ is the incidence angle of the ESCAT measurement and $\theta_{(\mathrm{PR})}$ is the incidence angle of ith TRMM PR measurement. The attenuation observed by ESCAT α_{atm} is calculated by averaging $\alpha_{\mathrm{PR}}(i)$ over the ESCAT footprint using (5). The ESCAT-observed PIA $\mathrm{PIA}_{\mathrm{atm}}$ is

$$\mathrm{PIA}_{\mathrm{atm}} = -10\log_{10}\alpha_{\mathrm{atm}}. \tag{8}$$

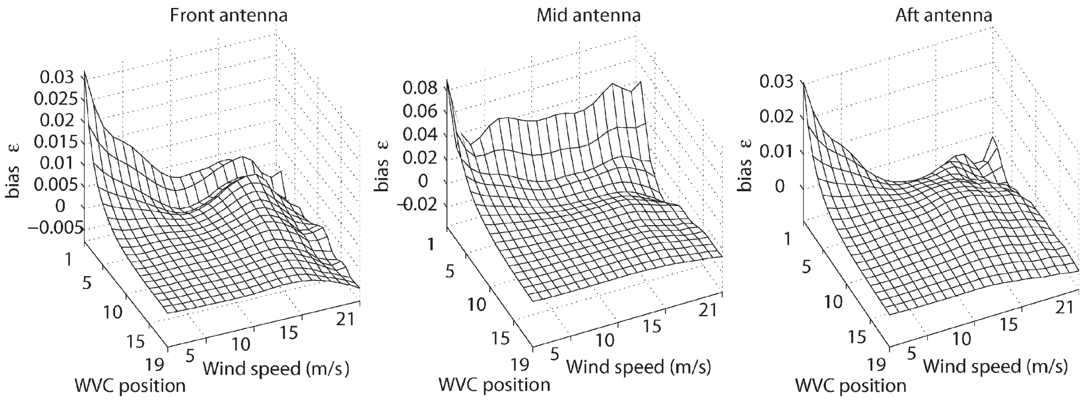

Fig. 3. Mean biases between ECMWF-predicted σ° and ERS scatterometer-measured σ° for fore, mid, and aft antennas at different cross-swath WVC positions and different wind-speed bins.

ESCAT atmospheric backscatter ($\sigma_{\rm atm}$) is estimated by the following procedure. First, the effective reflectivity of the atmospheric rain ($Z_{\rm e}$) is calculated by the Z–R relation [14], [15]

$$Z_{\rm e} = AR^b \ {\rm mm}^6/{\rm m}^3 \tag{9}$$

where R is the TRMM PR level 2A25 3-D rain rate (millimeters per hour). The values of A and b depend on the type of rain. We assume typical stratiform rain value $A = 210$ and $b = 1.6$ [14] in this paper. The volume backscattering coefficient without atmospheric attenuation $\sigma_{\rm vc}(i)$ can be computed from [16]

$$\sigma_{\rm vc}(i) = 10^{-10}\frac{\pi^5}{\lambda_\circ^4}|K_{\rm w}|^2 Z_{\rm e} \ {\rm m}^{-1} \tag{10}$$

where $\lambda_\circ = 5.7$ cm is the wavelength of ESCAT and $|K_{\rm w}|^2$ is a function of the wavelength $\lambda_\circ$ and the physical temperature of the material. $K_{\rm w}$ is assumed to be 0.93 in this paper. The quantity $\sigma_{\rm vc}$ represents physically the backscattering cross section (square meters) per unit volume (cubic meters).

By following the method in [3], the volume backscatter cross section observed by the ESCAT is adjusted by the ESCAT-observed two-way atmospheric attenuation factor. The total atmospheric rain backscatter observed by the ESCAT at each TRMM PR measurement $\sigma_{\rm PR}(i)$ is then calculated by integrating the adjusted volume backscatter cross section through the PR antenna beam to the lowest no-surf-clutter range. The ESCAT-observed atmospheric backscatter $\sigma_{\rm atm}$ is calculated by averaging $\sigma_{\rm PR}(i)$ using (5).

The wind-induced surface backscatter $\sigma_{\rm wind}$ is estimated from colocated winds from ECMWF winds. As mentioned in Section II, the ECMWF wind fields are interpolated in time and space to the center of each ESCAT measurement using cubic spline interpolation of the zonal and meridional components of the wind. We compute the speed and direction of the wind in meteorological convention and calculate the σ° for three antennas of each ESCAT WVC through ERS GMF (CMOD5)

$$\sigma_{\rm wind(ECMWF)} = {\rm CMOD5}(s, d, \chi, \theta) \tag{11}$$

where the definition of the inputs of CMOD5 is the same as in (4). The wind-induced backscatter $\sigma_{\rm wind(ECMWF)}$ predicted by ECMWF has a bias ϵ introduced by prediction errors. Since the ECMWF wind fields are interpolated from low resolution to ESCAT resolution, the bias of ECMWF wind fields is spatially correlated in an ESCAT swath. To reduce the effect of the spatial correlation and contamination of rain on the measurements, we use a large data set (from January 1, 2000 to December 31, 2000) to estimate the ECMWF/ESCAT bias. The bias varies with incidence angle and antenna look direction, and it may change with wind speed and geophysical locations. Thus, we estimate ϵ for a specific look direction and incidence angle for each wind-speed bin by making a nonparametric estimate of $\epsilon = \sigma_{\rm m(ESCAT)} - \sigma_{\rm wind(ECMWF)}$ as a function of wind speed at evenly spaced wind-speed bins (from 0–20 m/s with a bin width of 1 m/s) by using an Epanechnikov kernel with a bandwidth of 3 m/s in wind speed. Only the colocated ECMWF and ESCAT data between latitude -40° and 40° are used to estimate the bias. Fig. 3 shows the mean of ϵ for fore, mid, and aft antennas at different cross-swath WVC positions and different wind-speed bins. Note that the bias is positive at low wind speed and is negative at high wind speed. The standard deviations of the bias ϵ for three antennas are less than 0.0074 for incidence angles greater than 40°. The estimate of wind-induced backscatter $\sigma_{\rm wind}$ is then represented by ECMWF-predicted wind-induced backscatter $\sigma_{\rm wind(ECMWF)}$ and bias ϵ

$$\sigma_{\rm wind} = \sigma_{\rm wind(ECMWF)} + \epsilon. \tag{12}$$

Based on the above parameters, we estimate the surface perturbation backscatter $\sigma_{\rm surf}$ by

$$\sigma_{\rm surf} = \alpha_{\rm atm}^{-1}(\sigma_{\rm m} - \sigma_{\rm atm}) - (\sigma_{\rm wind(ECMWF)} + \epsilon). \tag{13}$$

B. Selecting Model Function and Estimating Model Coefficients

We seek an empirical model function for (4). Power law (linear or quadratic log-log) models are sufficient to relate the three parameters with rain rate in Ku-band wind/rain backscatter model [3]. Similar functional forms work well at C-band.

Thus, $\alpha_{\rm atm}$, $\sigma_{\rm atm}$, and $\sigma_{\rm surf}$ for a specific incidence angle θ can be expressed as polynomial functions of rain rate

$$10\log_{10}(\mathrm{PIA}_{\rm atm}(\theta)) = 10\log_{10}(-10\log_{10}\alpha_{\rm atm}(\theta)) \approx f_a(R_{\rm dB}) = \sum_{n=0}^{N} x_a(n)R_{\rm dB}^n \quad (14)$$

$$10\log_{10}(\sigma_{\rm atm}(\theta)) \approx f_r(R_{\rm dB}) = \sum_{n=0}^{N} x_r(n)R_{\rm dB}^n \quad (15)$$

$$10\log_{10}(\sigma_{\rm surf}(\theta)) \approx f_{\rm sr}(R_{\rm dB}) = \sum_{n=0}^{N} x_{\rm sr}(n)R_{\rm dB}^n \quad (16)$$

where $R_{\rm dB} = 10\log_{10}(R_{\rm surf(ant)})$, $x_a(n)$, $x_r(n)$, and $x_{\rm sr}(n)$ are the corresponding model coefficients. $N = 1$ for the linear model, and $N = 2$ for the quadratic model. Because the estimate of $\sigma_{\rm surf}$ is relatively noisy and may be negative, we first make a nonparametric estimate of $\sigma_{\rm surf}$ as a function of $R_{\rm dB}$ at regular logarithmically spaced rain-rate bins using an Epanechnikov kernel [17] with a 3-dB bandwidth in $R_{\rm dB}$. Then, we estimate the model coefficients $x_{\rm sr}(n)$ for the linear/quadratic model using a robust linear least squares fit. We use a similar method in estimating $x_a(n)$ and $x_r(n)$. Since the atmospheric parameters and surface perturbation backscatter are uncorrelated with the azimuth look direction of the antenna, we combine the data from all antennas during the coefficient estimation. To ensure sufficient data for each model fit, we use an incidence-angle bin size approximately equal to 4°. Because the incidence angles of the ESCAT measurements are not uniformly distributed, the bin size is slightly increased where measurements at the incidence-angle range are more rare.

In the analysis, we observe that for incidence angles less than 30°, the surface rain perturbation is not a monotonic function of surface rain rate. It cannot adequately be modeled by a linear or quadratic model. A hypothesis for the reason is that the contributions of ring waves and upper surface turbulence are comparable under such conditions. For incidence angles greater than 30°, the surface rain perturbation is monotonically increasing with surface rain rate, suggesting that the contribution of ring waves dominates the surface effects of rain. We note that the Bragg wavelength of ESCAT at incidence angles higher than 30° is shorter than 5.8 cm, which is close to the wavelength condition mentioned previously. For incidence angles between 30° and 40°, the variance of the estimation of $\sigma_{\rm surf}$ is relatively large, which makes the model coefficients unreliable. Thus, in this paper, we only describe the model coefficients for incidence angles greater than 40°. It is noted that due to the inhomogeneity of rain events in an ESCAT footprint, only the total surface effect of rain in the backscatter measurements can be described by the model.

Graphics showing the nonparametric fits to the estimated $\mathrm{PIA}_{\rm atm}(\theta)$ and $\sigma_{\rm atm}(\theta)$ with respect to $R_{\rm dB}$ for incidence angles between 40° and 57° are shown in Figs. 4 and 5. The dashed line is the nonparametric fit. The corresponding estimated coefficients for $x_a(n)$ and $x_r(n)$ for both robust fit and quadratic fit are given in Tables I and II. From these two tables, we note that all the second-order coefficients of the quadratic

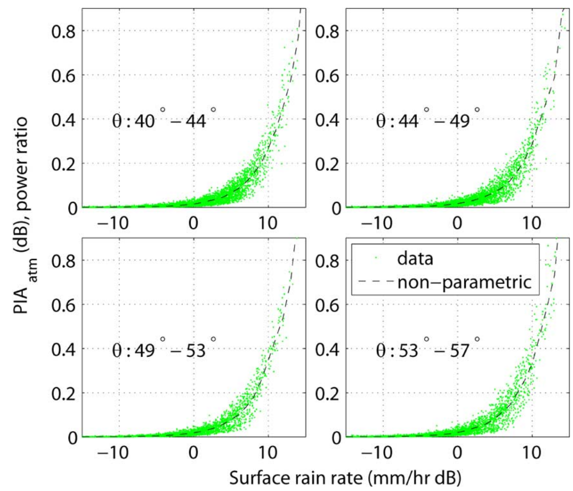

Fig. 4. Nonparameric fit to estimated $\mathrm{PIA}_{\rm atm}(\theta)$ with respect to $R_{\rm dB}$ for different incidence-angle bins. Estimated PIA is displayed in scatter plot. $R_{\rm dB}$ is between −15 and 15 dB.

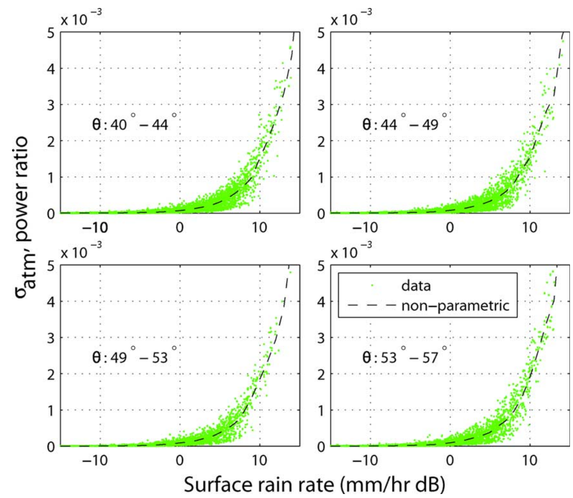

Fig. 5. Nonparameric fit to estimated $\sigma_{\rm atm}(\theta)$ with respect to $R_{\rm dB}$ for different incidence-angle bins. Estimated $\sigma_{\rm atm}$ is in normal space, which is displayed in scatter plot. $R_{\rm dB}$ is between −15 and 15 dB.

TABLE I
C-BAND MODEL COEFFICIENTS (LINEAR AND QUADRATIC) OF $\mathrm{PIA}_{\rm atm}(\theta)$

θ (°)		$x_a(0)$	$x_a(1)$	$x_a(2)$
40-44	Linear	-18.23	1.25	
	Quadratic	-18.18	1.25	-0.00060
44-49	Linear	-17.89	1.25	
	Quadratic	-17.79	1.24	-0.0016
49-53	Linear	-17.44	1.26	
	Quadratic	-17.39	1.25	-0.00081
43-57	Linear	-17.12	1.25	
	Quadratic	-17.05	1.24	-0.0012

TABLE II
C-BAND MODEL COEFFICIENTS (LINEAR AND QUADRATIC) OF $\sigma_{\rm atm}(\theta)$

θ (°)		$x_r(0)$	$x_r(1)$	$x_r(2)$
40-44	Linear	-41.79	1.33	
	Quadratic	-41.76	1.33	-0.00030
44-49	Linear	-41.46	1.32	
	Quadratic	-41.44	1.32	-0.00020
49-53	Linear	-41.03	1.33	
	Quadratic	-41.07	1.33	0.00090
53-57	Linear	-40.69	1.32	
	Quadratic	-40.66	1.32	-0.00060

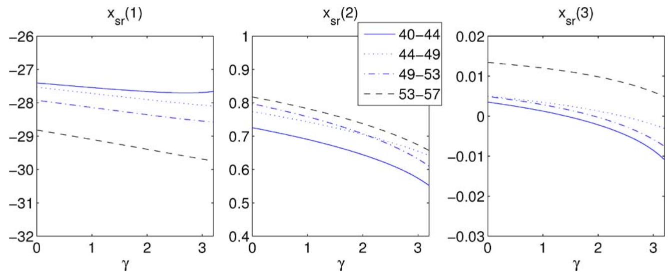

Fig. 6. $x_{\mathrm{sr}}(n)$ for the quadratic model as a function of the rain backscatter calibration parameter γ for different incidence-angle ranges.

model are negligibly small, suggesting that $\mathrm{PIA}_{\mathrm{atm}}(\theta)$ and $\sigma_{\mathrm{atm}}(\theta)$ are almost a linear function of surface rain rate in log-log space.

In the derivation of $\sigma_{\mathrm{surf}}(\theta)$, error is introduced by several sources. One of them is the prediction error of the ECMWF predicted wind-induced backscatter σ_{wind}. The procedure for estimating α_{atm} and σ_{atm} from the TRMM PR level 2A25 3-D rain rate introduces additional errors due to the error of the empirical model functions, NUBF, and the temporal and spatial mismatch of ESCAT and TRMM PR measurements. We do not analyze all these errors in detail here. Instead, we evaluate the sensitivity of $\sigma_{\mathrm{surf}}(\theta)$ to the error introduced by σ_{atm}. We adopt the combined rain model of (2) to reduce the influence of the error.

To evaluate the sensitivity of $\sigma_{\mathrm{surf}}(\theta)$ to σ_{atm}, following the study in [3], we introduce a variable calibration parameter γ to (13)

$$\sigma_{\mathrm{surf}} = \alpha_{\mathrm{atm}}^{-1}(\sigma_{\mathrm{m}} - \gamma\sigma_{\mathrm{atm}}) - \left(\sigma_{\mathrm{wind(ECMWF)}} + \epsilon\right). \quad (17)$$

Using the method described above, we calculate the linear/quadratic model coefficients of $\sigma_{\mathrm{surf}}(\theta)$ for each γ between 0 and 3.2 with a step of 0.1. When γ is greater than 3.2, $\sigma_{\mathrm{surf}}(\theta)$ may become negative. We pick the optimum γ by defining a least squares objective function $f(\gamma)$ with respect to γ

$$f(\gamma) = \sum_i \left(\sigma_{\mathrm{m}}^i - \sigma_{\mathrm{m(model)}}^i(\gamma)\right)^2 \quad (18)$$

where i is the ith data in the data set and $\sigma_{\mathrm{m(model)}}(\gamma)$ is the σ° calculated with the quadratic model coefficients with respect to the corresponding γ. The value of γ that minimizes $f(\gamma)$ is the optimum value γ_{opt}. For all the measurements with incidence angles between 40° and 57°, $\gamma_{\mathrm{opt}} = 1.2$, suggesting that the estimates of σ_{atm} are slightly underestimated. The estimated coefficients of $\sigma_{\mathrm{surf}}(\theta)$ are plotted as a function of the calibration parameter γ for different incidence-angle bins in Fig. 6. We note that none of the three terms are particularly sensitive to the value of γ, suggesting that the influence of the σ_{atm}-induced error is insignificant as expected. We list the values of $x_{\mathrm{sr}}(n)$ corresponding to γ_{opt} in Table III. Compared with the counterparts in Table II, it is noted that the constant term of $\sigma_{\mathrm{surf}}(\theta)$ is significantly higher than the constant term of $\sigma_{\mathrm{atm}}(\theta)$, while the linear and quadratic terms of $\sigma_{\mathrm{surf}}(\theta)$ are on the same order of magnitude as the linear and quadratic terms of $\sigma_{\mathrm{atm}}(\theta)$.

TABLE III
MODEL COEFFICIENTS OF SURFACE PERTURBATION BACKSCATTER $\sigma_{\mathrm{surf}}(\theta)$

θ		$xsr(0)$	$xsr(1)$	$xsr(2)$
40-44	Linear	-27.45	0.68	
	Quadratic	-27.78	0.7	0.0004
44-49	Linear	-27.59	0.74	
	Quadratic	-27.85	0.74	0.0031
49-53	Linear	-28.13	0.769	
	Quadratic	-28.24	0.74	0.0031
53-57	Linear	-28.582	0.846	
	Quadratic	-29.14	0.773	0.0116

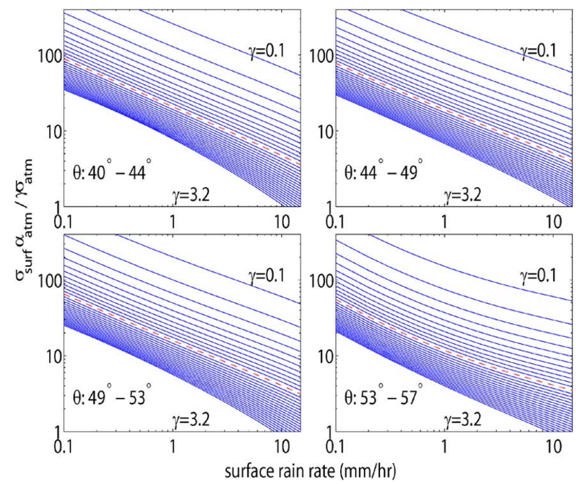

Fig. 7. Ratio of the attenuated surface perturbation $\alpha_{\mathrm{atm}}\sigma_{\mathrm{surf}}(\theta)$ to the calibrated atmospheric rain backscatter $\gamma\sigma_{\mathrm{atm}}$ for different γ in the range of 0.1–3.2 with a step of 0.1 separately plotted as a function of rain rate for several incidence-angle ranges. Dashed line corresponds to γ_{opt}.

To further compare the contribution of the surface perturbation and the atmospheric backscatter, we compute the ratio of the attenuated surface perturbation $\alpha_{\mathrm{atm}}\sigma_{\mathrm{surf}}(\theta)$ to the calibrated atmospheric rain backscatter $\gamma\sigma_{\mathrm{atm}}(\theta)$ with respect to R_{dB} for different incidence-angle bins, which is shown in Fig. 7. For γ_{opt}, the ratio $\alpha_{\mathrm{atm}}\sigma_{\mathrm{surf}}/\gamma\sigma_{\mathrm{atm}}(\theta)$ for different θ is always greater than three, suggesting that the surface rain backscatter always dominates the total rain-induced backscatter (but not necessarily the total backscatter).

It is noted that we only care about the total effect of rain in wind retrieval. The corresponding power law model of σ_{eff} is

$$10\log_{10}\left(\sigma_{\mathrm{eff}}(\theta)\right) \approx f_{\mathrm{e}}(R_{\mathrm{dB}}) = \sum_{n=0}^{N} x_{\mathrm{e}}(n) R_{\mathrm{dB}}^n. \quad (19)$$

The coefficients of $x_{\mathrm{e}}(n)$ are calculated using the same method mentioned before, shown in Table IV, and plotted in Fig. 8. The estimated $\sigma_{\mathrm{eff}}(\theta)$ is shown in the density plot. The dashed line is the nonparametric fit. Fig. 9 shows the nonparametric fit and linear/quadratic fits in log-log space.

We further investigate the relationship between $\sigma_{\mathrm{eff}}(\theta)$ and incidence angle θ by plotting the $\sigma_{\mathrm{eff}}(\theta)$ with respect to θ for a specific surface rain rate in Fig. 10. We use the quadratic model coefficients to estimate $\sigma_{\mathrm{eff}}(\theta)$ for θ between 40° and 57°. At a low rain rate, the magnitude of σ_{eff} generally decreases with incidence angle. At a moderate rain rate, the σ_{eff} almost remains constant for all incidence angles. At a heavy rain rate,

TABLE IV
MODEL COEFFICIENTS OF EFFECTIVE RAIN BACKSCATTER $\sigma_{\mathrm{eff}}(\theta)$

θ		$x_{eff}(0)$	$xe(1)$	$xe(2)$
40-44	Linear	-27.21	0.703	
	Quadratic	-27.60	0.728	0.0016
44-49	Linear	-27.37	0.759	
	Quadratic	-27.61	0.76	0.0030
49-53	Linear	-27.87	0.797	
	Quadratic	-27.96	0.768	0.0034
53-57	Linear	-28.19	0.851	
	Quadratic	-28.78	0.791	0.0109

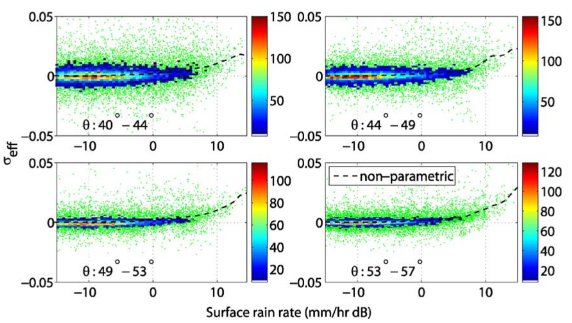

Fig. 8. Nonparametric fits to the effective rain backscatter σ_{eff} in log-normal space for different incidence-angle bins. The dashed line is the nonparametric fit. Data are shown in a density plot.

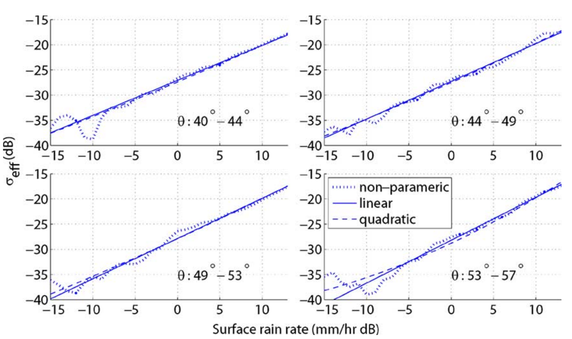

Fig. 9. Linear and quadratic fits to the nonparametric fits of effective rain backscatter σ_{eff} in log-normal space for different incidence-angle bins. Nonparametric fits are also plotted.

σ_{eff} increases with incidence angle. It is also noted that wind-induced backscatter $\sigma_{\mathrm{wind}}(\theta)$ decreases with incidence angle. Thus, rain-induced backscatter has more impact on the C-band scatterometer measurements at high incidence angle than at low incidence angle.

IV. MODEL VALIDATION AND DATA REGIMES

In this section, we validate the rain/wind model by comparing the model-estimated backscatter $\sigma_{\mathrm{m(model)}}(\theta)$ to the actual ESCAT backscatter measurements $\sigma_{\mathrm{m(ESCAT)}}(\theta)$ for different surface rain-rate bins in Figs. 11 and 12. $\sigma_{\mathrm{m(model)}}(\theta)$ is estimated using the quadratic model. To illustrate the difference in using the wind/rain model, we also show a scatter plot of $\sigma_{\mathrm{m(ESCAT)}}(\theta)$ with respect to ECMWF-predicted wind-only backscatter $\sigma_{\mathrm{wind(ECMWF)}}(\theta) + \epsilon$ for the same rain-rate bin and incidence-angle bin in Figs. 13 and 14. It is noted that rain introduces a bias to the backscatter, with the bias increasing with rain rate and incidence angle. After applying the wind/rain

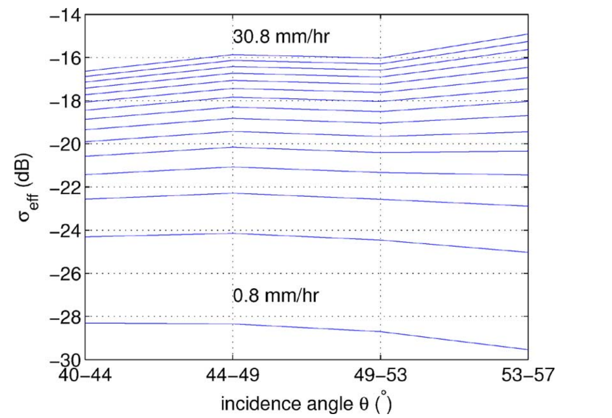

Fig. 10. Relationship between $\sigma_{\mathrm{eff}}(\theta)$ and incidence angle for several surface rain rates (millimeters per hour). Rain rates range from 0.8 to 30.8 mm/h with a step of 1 mm/h.

model, the rain-induced bias is eliminated. For θ ranging from 40° to 49°, 95% of the model-predicted backscatter is within 3 dB of the ESCAT-measured backscatter, while the standard deviation of log error, $\sigma_{\mathrm{m(model)}}(\theta) - \sigma_{\mathrm{m(ESCAT)}}(\theta)$, is 1.4 dB. For θ ranging from 49° to 57°, the percentage is 91% and the standard deviation is 1.6 dB.

To further validate the model, we compute a nonparametric estimate of both $\sigma_{\mathrm{m(ESCAT)}}(\theta)$ and $\sigma_{\mathrm{m(model)}}(\theta)$ on a regular grid with axes of $\sigma_{\mathrm{wind(ECMWF)}} + \epsilon$ and R_{dB} using a 2-D Epanechnikov kernel with a bandwidth of 3 dB for different incidence-angle bins. $\sigma_{\mathrm{m(model)}}(\theta)$ is calculated using the quadratic combined rain model. The log error is computed as $\sigma_{\mathrm{m(model)}}(\theta) - \sigma_{\mathrm{m(ESCAT)}}(\theta)$ in decibels. Fig. 15 shows nonparametric estimates of $\sigma_{\mathrm{m(ESCAT)}}(\theta)$, $\sigma_{\mathrm{m(model)}}(\theta)$, and the log error with respect to $\sigma_{\mathrm{wind(ECMWF)}} + \epsilon$ and the surface rain rate (millimeters per hour per decibel) for different incidence-angle bins. For the two incidence-angle bins shown, the model-estimated backscatter is very close to the ESCAT-measured backscatter, with a log error within ± 2 dB. It is noted that the largest error occurs at high rain rates due to less data.

To understand the effect of rain on the scatterometer measurements for different incidence angles, following the study in [3], we define three distinct backscatter regimes. In regime 1, rain-induced backscatter dominates the total backscatter. Regime 2 is where the rain-induced backscatter and the wind-induced backscatter are on the same order of magnitude. In regime 3, wind-induced backscatter dominates the total backscatter. It is noted that wind and rain information may be simultaneously retrieved from regime 2, while in regime 1 or regime 3, only the dominating parameter (wind or rain) can be retrieved. We identify these regimes by thresholding the ratio $\tau = \sigma_{\mathrm{eff}}/\sigma_{\mathrm{m}}$. We define regime 1 by $\tau > 0.75$, regime 3 as $\tau < 0.25$, and regime 2 as $0.75 \geq \tau \geq 0.25$. In Fig. 16, we plot the τ computed using the combined wind/rain model with respect to surface rain rate R_{dB} and wind-only backscatter σ_{wind}, with the three regimes shown in different colors. We also plot contours of the predicted total backscatter σ_{m}. We choose the range of σ_{wind} for different incidence angles using three standard deviations from the mean, accounting for roughly 95% of the colocated data set. It is noted that with the increasing of surface rain rate, the curve of σ_{m} deviates from the curve of

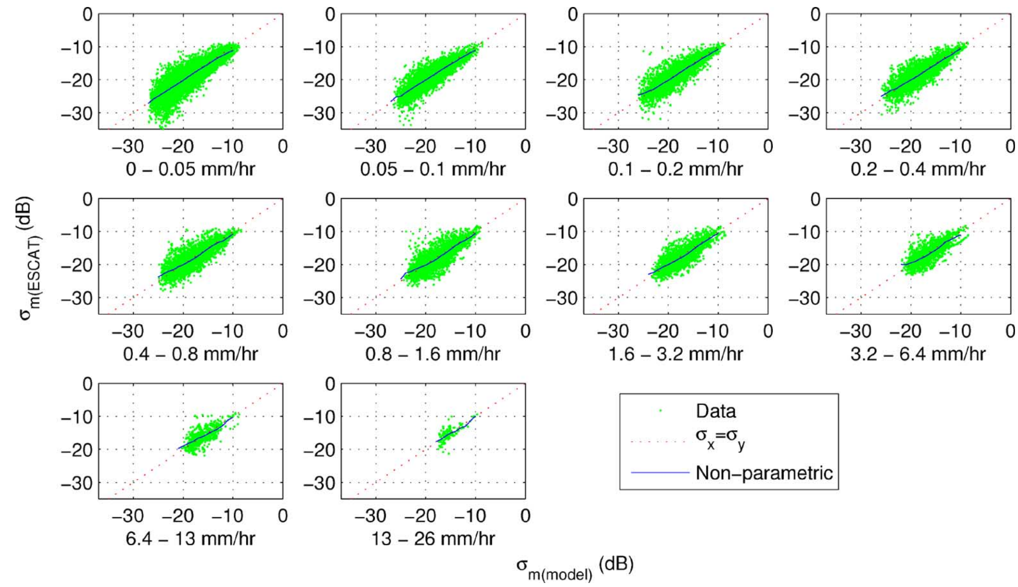

Fig. 11. ESCAT-measured backscatter $\sigma_{\mathrm{m(ESCAT)}}$ plotted as a function of model-estimated backscatter $\sigma_{\mathrm{m(model)}}$ with the quadratic model for incidence angles 40°–49° for different rain-rate bins. A nonparametric fit is also plotted.

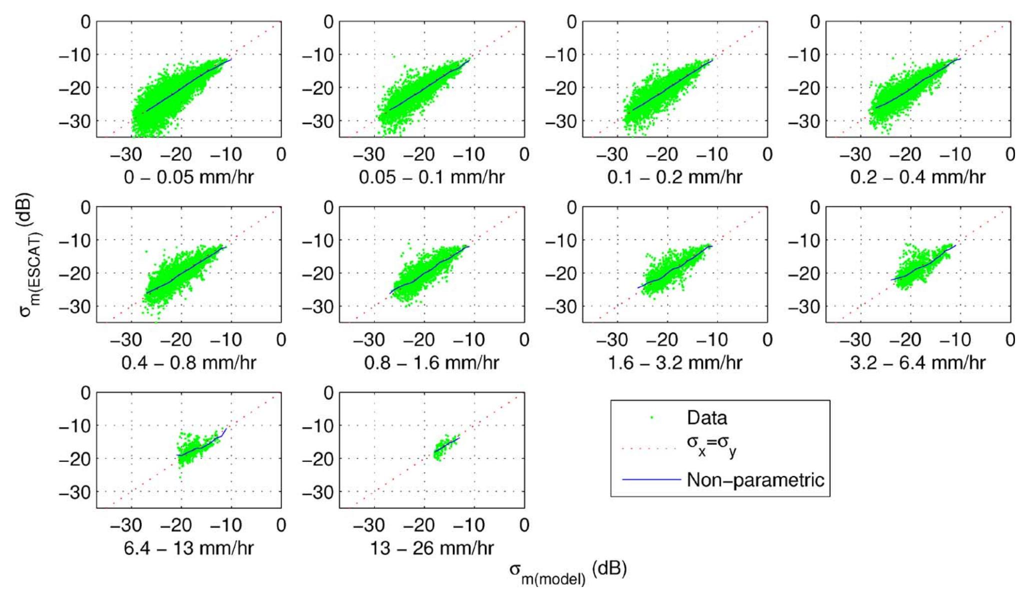

Fig. 12. ESCAT-measured backscatter $\sigma_{\mathrm{m(ESCAT)}}$ plotted as a function of model-estimated backscatter $\sigma_{\mathrm{m(model)}}$ with the quadratic model for incidence angles 49°–57° for different rain-rate bins. A nonparametric fit is also plotted.

σ_{wind}. As the incidence angle increases, the area of regime 1 reduces while the area of regime 3 increases, suggesting that rain has more significant impact on the ESCAT measurements at higher incidence angles.

We further investigate this by computing the percentage of colocated measurements falling in each regime with significant rain ($\geq$ 0.8 mm/h) and ECMWF wind speed greater than 2 m/s, listed in Table V. It is noted that about 3% of all the colocated ESCAT measurements observe significant rain ($\geq$ 0.8 mm/h). To investigate the relationship between the data regimes, wind speed, and rain rate, we plot mean τ with respect to the ECMWF-predicted wind speed and average surface rain rate (millimeters per hour) for all the colocated measurements with significant rain ($\geq$ 0.8 mm/h) and ECMWF wind speed greater than 2 m/s in Fig. 17, with a bin width of 4 m/s for wind speed and a bin width of 4 mm/h for surface rain rate. It is noted that regime 1 ($\tau > 0.75$) mostly happens at low wind speed and high rain conditions, suggesting that rain has a significant impact on the total backscatter in such conditions.

V. Conclusion

With the confirmed existence of rain surface perturbation by recent studies, the rain effect on C-band scatterometer measurements needs to be reevaluated. By using colocated TRMM PR, ESCAT on ERS, and ECMWF data, we develop and evaluate a simple low-order wind/rain backscatter model which inputs surface rain rate, incidence angle, wind speed, wind direction, and azimuth angle. By applying the model to the colocated data set, we demonstrate that the wind/rain backscatter model is

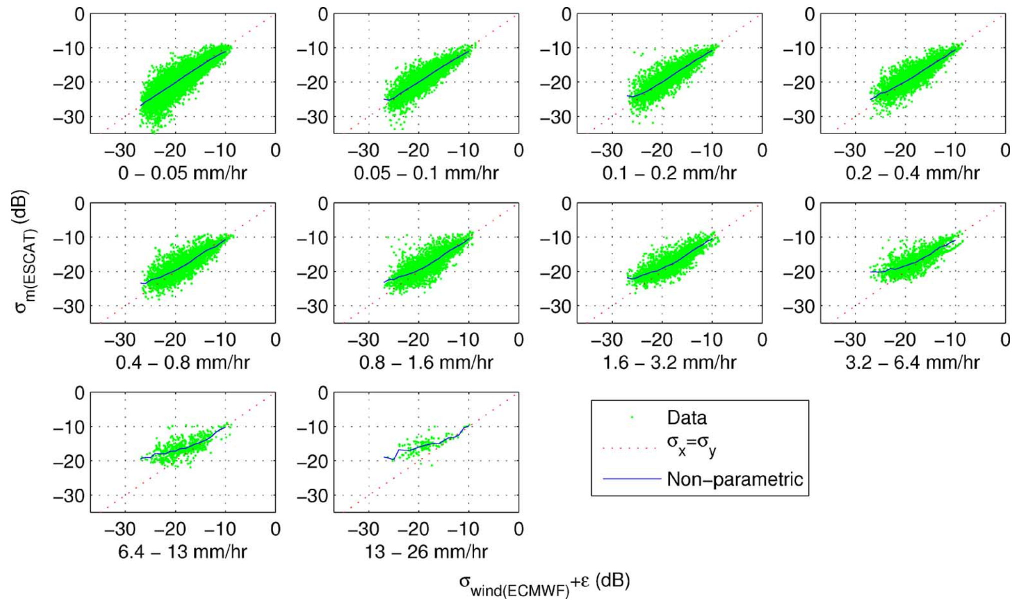

Fig. 13. ESCAT-measured backscatter $\sigma_{\rm m(ESCAT)}$ plotted as a function of wind-only backscatter $\sigma_{\rm wind(ECMWF)} + \epsilon$ for incidence angles 40°–49° for different rain-rate bins. A nonparametric fit is also plotted.

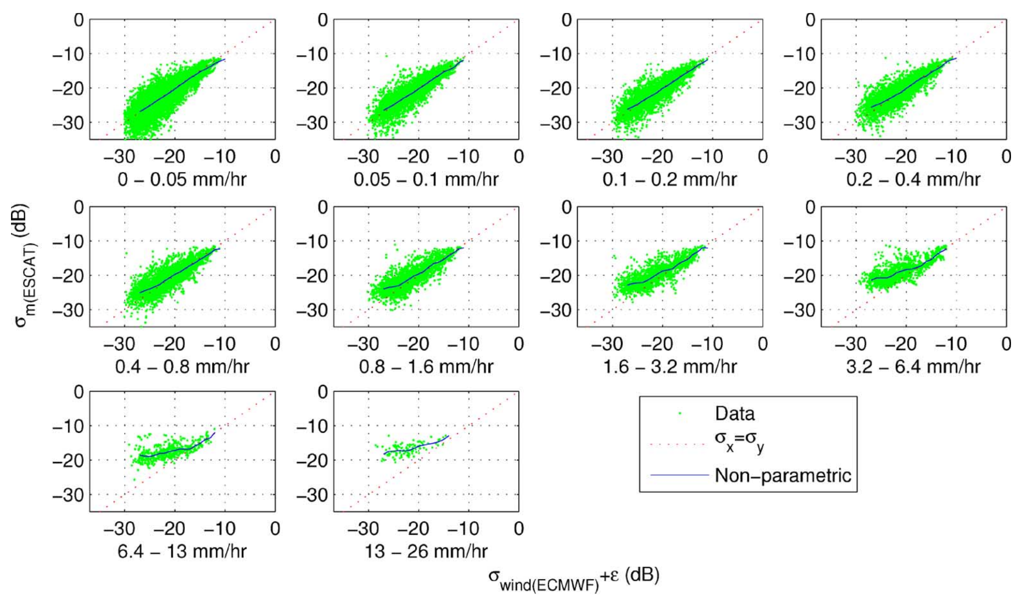

Fig. 14. ESCAT-measured backscatter $\sigma_{\rm m(ESCAT)}$ plotted as a function of wind-only backscatter $\sigma_{\rm wind(ECMWF)} + \epsilon$ for incidence angles 49°–57° for different rain-rate bins. A nonparametric fit is also plotted.

accurate enough for describing the total backscatter in raining areas with relatively low variance. We also show that the rain surface perturbation is a dominating factor of the rain-induced backscatter.

Using three distinct regimes, we identify under what conditions the wind and rain can be retrieved from the measurements. In regime 1 where rain dominates, only rain information may be retrieved from the measurements. In regime 3 where wind dominates, only wind information can be retrieved. In regime 2 where rain and wind are comparable, wind and rain information may be simultaneously retrieved from the measurements. In regime 1 and regime 2, the current wind retrieval methods are inadequate to retrieve the correct wind information. Therefore, the rain model should be incorporated into the retrieval algorithm. For incidence-angle bins 40° to 44°, 44° to 49°, 49° to 53°, and 53° to 57°, about 0.9%, 1.3%, 1.74%, and 1.67% of all the colocated ESCAT measurements are affected by rain (falling in regime 1 or 2).

We also show that rain has more impact on the C-band measurements at higher incidence angles. Since the successor of ESCAT on ERS, the advanced scatterometer instrument (ASCAT) on MetOp has incidence angles ranging from 25° to 65°, the measurements of ASCAT are expected to be more sensitive to rain than ESCAT on ERS.

Due to beam-filling effect and variance of the ECMWF predicted $\sigma°$, relative large variance is shown in the model for

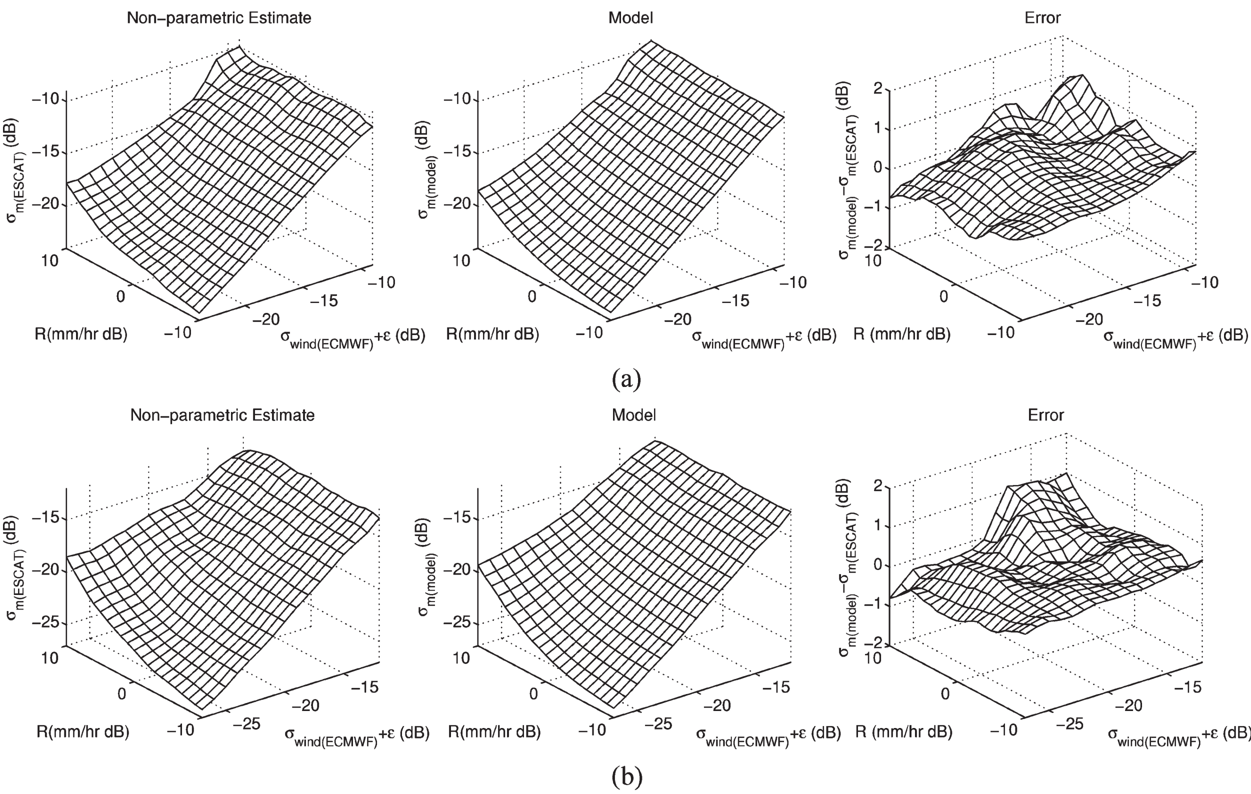

Fig. 15. Nonparametric estimates of $\sigma_{\mathrm{m(ESCAT)}}(\theta)$, $\sigma_{\mathrm{m(model)}}(\theta)$, and the difference are plotted with respect to $\sigma_{\mathrm{wind(ECMWF)}} + \epsilon$ and surface rain rate R(mm/h · dB) for incidence angles in range of (a) 40°–49° and (b) 49°–57°.

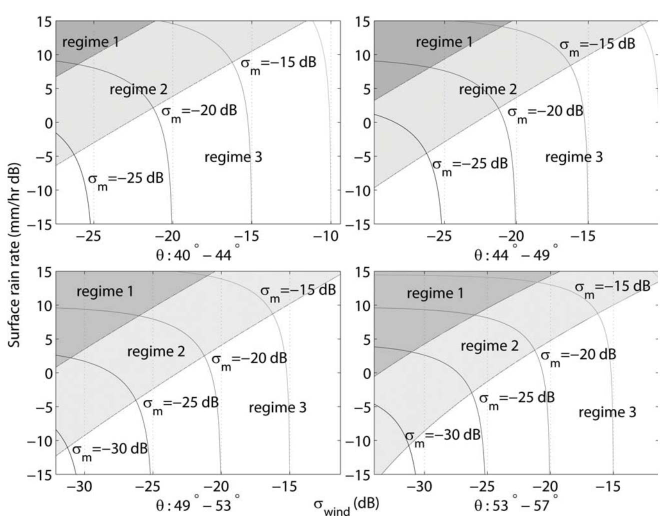

Fig. 16. Backscatter regimes for ESCAT as a function of rain rate and effective wind backscatter for several incidence angles. Also plotted is a contour plot of the combined rain effect model for σ_{m} (solid lines) and σ_{wind} (dotted lines).

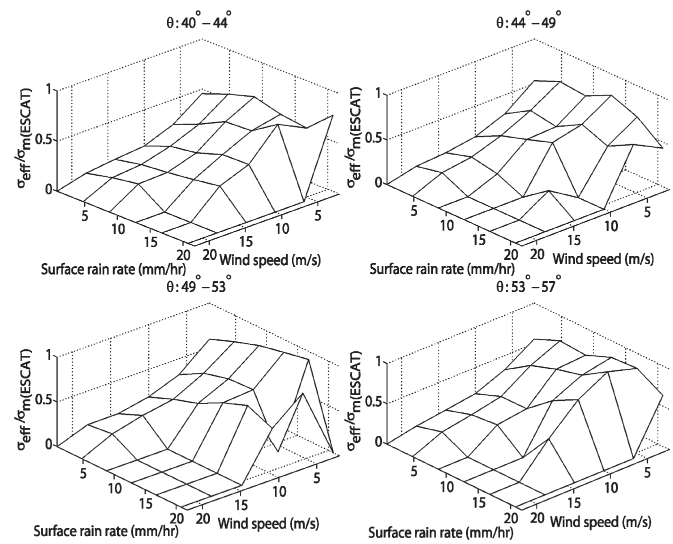

Fig. 17. Mean $\sigma_{\mathrm{eff}}/\sigma_{\mathrm{m}}$ with respect to ECMWF-predicted wind speed and TRMM PR-measured surface rain rate for different incidence-angle bins. The wind speed ranges from 2–22 m/s with a bin width of 4 m/s. The surface rain rate ranges from 0.8–20.8 mm/h with a bin width of 4 mm/h.

TABLE V
PERCENTAGE FALLING IN EACH REGIME OF COLOCATED MEASUREMENTS WITH SIGNIFICANT RAIN ($\geq$ 0.8 mm/h) AND ECMWF WIND SPEED GREATER THAN 2 m/s. THIS REPRESENTS 3% OF THE TOTAL DATA

$\theta(^\circ)$	Regime 1	Regime 2	Regime 3
40-44	0.64%	27.38%	71.98%
44-49	2.27%	41.38%	56.35%
49-53	5.17%	52.87%	41.96%
53-57	5.75%	49.74%	44.51%

low rain data. But, the majority of the data (95% for 40° to 49° and 91% for 49° to 57°) lie within 3 dB of the model. This illustrates how well the model performs. In fact, ESCAT retrieved wind vectors are mainly affected by mid-to-heavy rain at high incidence angles. The model is expected to retrieve rain rate and improve the retrieved wind vector in such situations. A following paper will explore this in great detail.

ACKNOWLEDGMENT

The authors would like to thank R. Halterman for his assistance in colocating the ESCAT/TRMM PR data.

REFERENCES

[1] I. I. Lin, D. Kasilingam, W. Alpers, T. K. Lim, H. Lim, and V. Khoo, "A quantitative study of tropical rain cells from ERS SAR imagery," in *Proc. Int. Geosci. and Remote Sens. Symp.*, Singapore, 1997, pp. 1527–1529.

[2] D. Kasilingam, I. I. Lin, H. Lim, V. Khoo, W. Alpers, and T. K. Lim, "Investigation of tropical rain cells with ERS SAR imagery and ground-based weather radar," in *Proc. 3rd ERS Symp.*, 1997, pp. 1603–1608.

[3] D. W. Draper and D. G. Long, "Evaluating the effect of rain on SeaWinds scatterometer measurements," *J. Geophys. Res.*, vol. 109, no. C12, pp. C02005.1–C02005.12, Feb. 2004.

[4] N. Braun, M. Gade, and P. A. Lange, "Radar backscattering measurements of artificial rain impinging on a water surface at different wind speeds," in *Proc. Int. Geosci. and Remote Sens. Symp.*, Hamburg, Germany, 1999, pp. 1963–1965.

[5] C. Melsheimer, W. Alpers, and M. Gade, "Simultaneous observations of rain cells over the ocean by the synthetic aperture radar aboard the ERS satellites and by surface-based weather radars," *J. Geophys. Res.*, vol. 106, no. C3, pp. 4665–4677, Mar. 2001.

[6] M. H. Freilich and R. S. Dunbar, "Derivation of satellite wind model functions using operational surface wind analyses: An altimeter example," *J. Geophys. Res.*, vol. 98, no. C8, pp. 14 633–14 649, Aug. 1993.

[7] L. F. Bliven, P. W. Sobieski, and C. Craeye, "Rain generated ring-waves: Measurements and modeling for remote sensing," *Int. J. Remote Sens.*, vol. 18, no. 1, pp. 221–228, Jan. 1997.

[8] L. F. Bliven, J. P. Giovanangeli, and G. Norcross, "Scatterometer directional response during rain," in *Proc. IEEE Int. Geosci. Remote Sens. Symp.*, 1989, pp. 1887–1890.

[9] A. Persson and F. Grazzini, *User Guide to ECMWF Forecast Products*. Reading, U.K.: Eur. Centre Medium Range Weather Forecasts, 2005.

[10] E. Attema, "The Active Microwave Instrument onboard the ERS-1 satellite," *Proc. IEEE*, vol. 79, no. 6, pp. 791–799, Jun. 1991.

[11] H. Hersbach, "CMOD5—An improved geophysical model function for ERS C-band scatterometry," ECMWF, Reading, U.K., ECMWF Tech. Memo. No. 395, 2003.

[12] T. Kozu, T. Kawanishi, H. Kuroiwa *et al.*, "Development of precipitation radar on-board the Tropical Rainfall Measuring Mission (TRMM) satellite," *IEEE Trans. Geosci. Remote Sens.*, vol. 39, no. 1, pp. 102–116, Jan. 2001.

[13] T. Iguchi, T. Kozu, R. Meneghini, J. Awaka, and K. Okamoto, "Rain profiling algorithm for the TRMM Precipitation Radar," *J. Appl. Meteorol.*, vol. 39, no. 12, pp. 2038–2052, Dec. 2000.

[14] L. J. Battan, *Radar Observation of the Atmosphere*. Chicago, IL: Univ. Chicago Press, 1973.

[15] R. J. Doviak and D. S. Zrnic, *Doppler Radar and Weather Observations*. San Diego, CA: Academic, 1984.

[16] F. T. Ulaby, R. K. Moore, and A. K. Fung, *Microwave Remote Sensing: Active and Passive*, vol. II. Reading, MA: Artech House, 1982.

[17] M. P. Wand and M. C. Jones, *Kernel Smoothing*. London, U.K.: Chapman & Hall, 1995.

Congling Nie (S'06) received the B.S. degree in electrical engineering from the South China University of Technology, Guangzhou, China, in 1995. He is currently working toward the Ph.D. degree in electrical engineering at Brigham Young University (BYU), Provo, UT.

From 1995 to 2003, he was with the Meteorological Center of Central and South China Air Traffic Management Bureau, where he developed weather radar applications for air traffic control. He joined the Microwave Earth Remote Sensing Research Group at BYU, Provo, UT, in 2003. His current research interests include rain effects on microwave backscatter from ocean surfaces and scatterometer wind retrieval.

David G. Long (S'80–M'82–SM'98) received the Ph.D. degree in electrical engineering from the University of Southern California, Los Angeles, in 1989.

From 1983 to 1990, he worked with NASA's Jet Propulsion Laboratory (JPL) where he developed advanced radar remote sensing systems. While with JPL, he was the Project Engineer on the NASA Scatterometer (NSCAT) project, which flew from 1996 to 1997. He also managed the SCANSCAT project, the precursor to SeaWinds, which was launched in 1999 and 2002. He is currently a Professor with the Electrical and Computer Engineering Department at Brigham Young University (BYU), Provo, UT, where he teaches upper division and graduate courses in communications, microwave remote sensing, radar, and signal processing. He is the Director with the BYU Center for remote sensing. He is the Principal Investigator on several NASA-sponsored research projects in remote sensing. He has numerous publications in signal processing and radar scatterometry. His research interests include microwave remote sensing, radar theory, space-based sensing, estimation theory, signal processing, and mesoscale atmospheric dynamics. He has over 275 publications.

Dr. Long has received the NASA Certificate of Recognition several times. He is an Associate Editor of the IEEE GEOSCIENCE AND REMOTE SENSING LETTERS.